

APPLIED SCIENCES AND ENGINEERING

Localized concentration reversal of lithium during intercalation into nanoparticles

Wei Zhang,^{1*} Hui-Chia Yu,^{2*†} Lijun Wu,³ Hao Liu,^{4‡} Aziz Abdellahi,⁵ Bao Qiu,⁶ Jianming Bai,⁷ Bernardo Orvananos,² Fiona C. Strobridge,⁴ Xufeng Zhou,⁶ Zhaoping Liu,⁶ Gerbrand Ceder,⁸ Yimei Zhu,³ Katsuyo Thornton,^{2§} Clare P. Grey,⁴ Feng Wang^{1§}

Nanoparticulate electrodes, such as Li_xFePO_4 , have unique advantages over their microparticulate counterparts for the applications in Li-ion batteries because of the shortened diffusion path and access to nonequilibrium routes for fast Li incorporation, thus radically boosting power density of the electrodes. However, how Li intercalation occurs locally in a single nanoparticle of such materials remains unresolved because real-time observation at such a fine scale is still lacking. We report visualization of local Li intercalation via solid-solution transformation in individual Li_xFePO_4 nanoparticles, enabled by probing sub-angstrom changes in the lattice spacing in situ. The real-time observation reveals inhomogeneous intercalation, accompanied with an unexpected reversal of Li concentration at the nanometer scale. The origin of the reversal phenomenon is elucidated through phase-field simulations, and it is attributed to the presence of structurally different regions that have distinct chemical potential functions. The findings from this study provide a new perspective on the local intercalation dynamics in battery electrodes.

Li-ion batteries (LIBs) are preferred energy storage devices for portable electronics and are becoming important power sources for electric vehicles and grid-scale storage (1). In commercial battery electrodes, such as layered oxides (LiCoO_2 , $\text{LiCo}_{1/3}\text{Ni}_{1/3}\text{Mn}_{1/3}\text{O}_2$) (2, 3), spinel (LiMn_2O_4) (4), and olivine [LiFePO_4 (LFP)] (5), electrochemical reactions take place through an intercalation process, during which Li ions are inserted into interstitial sites of the host without causing significant structural changes in the electrodes (2, 6–10). Li intercalation can occur either through a two-phase transformation path (in which the fully lithiated phase nucleates and grows) or through a single-phase solid-solution transformation path (in which no phase boundaries form). Owing to the recent development of in situ probing techniques, significant progress has been made in understanding of intercalation dynamics and related phenomena in LIBs. Notably, direct observation from in situ studies revealed that in many of the material systems, especially nanoparticulate ones, fast Li incorporation may occur via nonequilibrium routes, radically boosting power density of the electrodes (6, 11–17).

Nanoparticulate electrodes, such as LFP, have unique advantages over their microparticulate counterparts for the applications in LIBs because of the shortened diffusion path and have been extensively investigated over the past decade (18). LFP is an important commercial

cathode material known for its superior safety and cycling stability. However, the origin of high-rate capability found in LFP has been a subject of debate because it is in conflict with the common belief of a sluggish two-phase transformation process in this material (19). Recent atomistic calculations predicted a nonequilibrium intercalation process that occurs via a single-phase solid-solution transformation during fast lithiation of nanosized LFP because of a low energy barrier for the transformation between LFP and FePO_4 (FP) (20). This nonequilibrium process provided the first explanation for the high-rate capability (11, 15, 20–24). The latest studies also showed that, even at low-to-moderate cycling rates, solid-solution states might still persist within broad, diffuse interfaces between LFP and FP phases (24–26). Moreover, the solid-solution transformation mechanism can lead to new electrochemical behaviors, such as Li redistribution between neighboring particles in multiparticle systems (19, 27–30). Similarly, Li redistribution may also occur in other electrode materials (31).

Compared to the significant progress in theory and modeling, experimental studies on electrochemical reactions in nanoparticulate LFP have lagged far behind, and no concrete evidence of solid-solution transformation was found until very recently, through fast in situ x-ray diffraction (XRD) measurements (11, 23). Another study via in situ scanning transmission x-ray microscopy (STXM) provided new evidence of solid-solution phase transformation even in micrometer-sized LFP particles, which identified ~100-nm-scale heterogeneity within particles (15). Yet, x-ray-based in situ techniques have spatial resolution for exploring local Li intercalation and the associated structural changes within individual nanoparticles (19, 27–30). High-resolution transmission electron microscopy (HRTEM) is capable of exceptional spatial resolution, and it has recently been developed for in situ tracking of the phase evolution, providing otherwise inaccessible details, such as the formation of misfit dislocations and solid-solution zones between FP and LFP during the two-phase transformation (26, 32). However, without the formation of distinctive phase boundaries during a monophasic solid-solution transformation in Li_xFePO_4 , the subtle change in lattice spacing, at the sub-angstrom scale, cannot be directly resolved by in situ HRTEM (26).

Here, we report advancement in in situ techniques enabling real-time tracking of Li intercalation in a single nanoparticle through electron diffraction (ED) and locally within nanosized domains via

Copyright © 2018
The Authors, some
rights reserved;
exclusive licensee
American Association
for the Advancement
of Science. No claim to
original U.S. Government
Works. Distributed
under a Creative
Commons Attribution
NonCommercial
License 4.0 (CC BY-NC).

¹Sustainable Energy Technologies Department, Brookhaven National Laboratory, Upton, NY 11973, USA. ²Department of Materials Science and Engineering, University of Michigan, Ann Arbor, MI 48109, USA. ³Condensed Matter Physics and Materials Science, Brookhaven National Laboratory, Upton, NY 11973, USA. ⁴Department of Chemistry, University of Cambridge, Lensfield Road, Cambridge CB2 1EW, UK. ⁵Department of Materials Science and Engineering, Massachusetts Institute of Technology, 77 Massachusetts Avenue, Cambridge, MA 02139, USA. ⁶Ningbo Institute of Materials Technology and Engineering, Chinese Academy of Sciences, Ningbo, 315201, P. R. China. ⁷National Synchrotron Light Source II, Brookhaven National Laboratory, Upton, NY 11973, USA. ⁸Department of Materials Science and Engineering, University of California, Berkeley, Berkeley, CA 94720, USA.

*These authors contributed equally to this work.

†Present address: Department of Computational Mathematics, Science and Engineering and Department of Chemical Engineering and Materials Science, Michigan State University, East Lansing, MI 48824, USA.

‡Present address: X-ray Science Division, Advanced Photon Source, Argonne National Laboratory, 9700 South Cass Avenue, Argonne, IL 60439, USA.

§Corresponding author. Email: kthorn@umich.edu (K.T.); fwang@bnl.gov (F.W.)

HRTEM imaging coupled with geometric phase analysis (GPA). Modification was made to the algorithm of GPA, making it suitable for in situ detection of sub-angstrom changes of lattice spacing (33). More specifically, a new function was integrated into GPA for processing time- and position-resolved lattice images, allowing for direct correlation of local displacement with the concentration of intercalated Li within a single solid-solution phase. Therefore, this method enables real-time visualization of the evolution of local Li concentration within a single nanoparticle, which is not achievable via ex situ measurements (34). Local Li intercalation dynamics in FP nanocrystals was visualized via this new approach, which revealed an inhomogeneous solid-solution transformation process within a single nanoparticle, accompanied with a surprising reversal of local Li concentration at the nanometer scale. Phase-field simulations were performed to elucidate the thermodynamic origin of the reversal phenomenon, which indicated that the presence of spatially varying chemical potential functions within the nanoparticle leads to such concentration reversal. The findings from this study provide new insights into local dynamics of electrochemically driven phase transformations within individual particles in intercalation-type battery electrodes.

RESULTS

Technique development for in situ tracking of local Li intercalation

Figure 1 illustrates the experimental setup for tracking local Li intercalation within individual FP nanoparticles. For this study, plate-shaped single-crystalline nanoparticles (shown in fig. S1A) were synthesized

through a solvothermal procedure (35) and coated with a thin carbon layer [characterized using electron energy-loss spectroscopy (EELS) mapping; Fig. 1A]. A TEM grid-based composite electrode was made of carbon-coated FP nanoparticles loaded on the carbon film (Fig. 1B), and during the measurements, could be connected to the Li-coated tip to activate electrochemical reactions under potentiostatic conditions (see details in Materials and Methods) (17). As shown in Fig. 1C, those TEM grid-based electrodes exhibited high-rate capability, comparable to that in normal composite electrodes (fig. S2) (35). FP nanoparticles were well dispersed on the TEM grids, and those isolated individuals were selected for in situ ED measurements with the electron beam along a certain zone axis (that is, b axis; parallel to the fast Li diffusion channel), as illustrated in Fig. 1B. In addition, this configuration allows tracking of local Li intercalation within a single FP particle, through high-resolution lattice imaging coupled with GPA analysis. With a modified GPA algorithm (see Materials and Methods), the lattice image taken from a selected area in the pristine sample (with lattice spacing a_{ref}) is used as the reference, and correspondingly, the evolution of lattice spacing as a function of time, $\Delta a(\mathbf{r}, t)$, relative to that of the pristine sample can be extracted from the subsequent lattice images

$$\Delta a(\mathbf{r}, t) = -a(\mathbf{r})a_{\text{ref}}\Delta \mathbf{g} \quad (1)$$

where $a(\mathbf{r})$ is the lattice spacing in the subsequent images taken from the selected area and $\Delta \mathbf{g}$ is the deviation from the ideal reciprocal lattice vector. Because of the strong correlation between lattice spacing and Li concentration in Li_xFePO_4 (11, 36), the two-dimensional (2D) lattice spacing maps generated as a function of time are highly sensitive to the

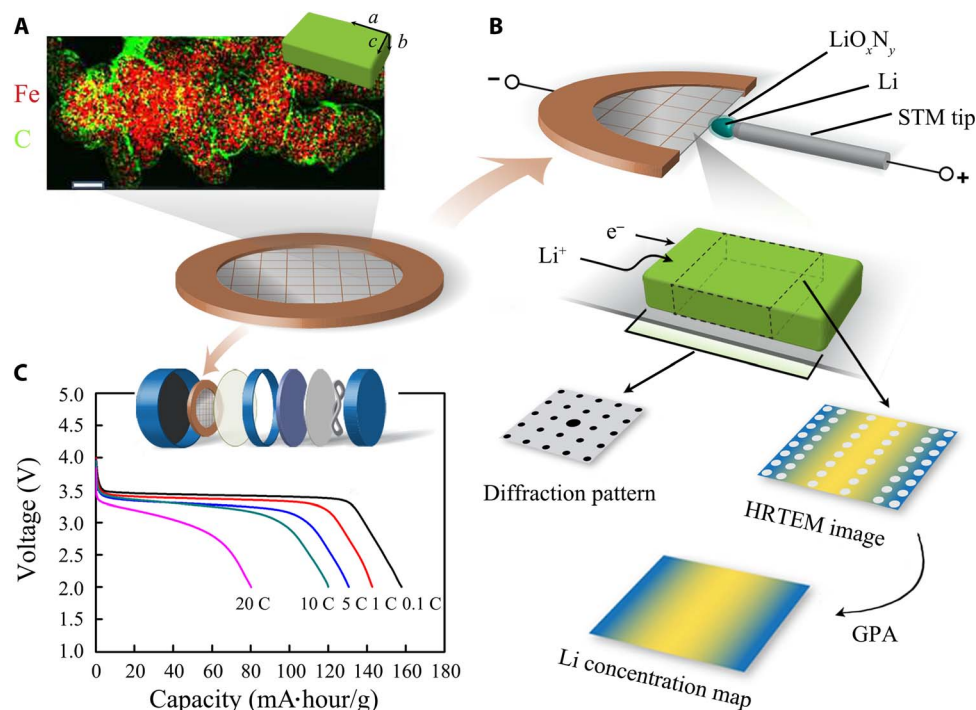


Fig. 1. Experimental setup for in situ tracking of local Li intercalation within a single-crystalline nanoparticle. (A) Chemical image of the representative FP nanoparticles for in situ measurements (mapped via EELS; Fe: red, C: green). The particles are plate-like single crystals, thin in the [010] crystalline axis (inset); scale bar, 100 nm. (B) Schematic illustration of the in situ electrochemical cell containing a half-TEM grid loaded with FP nanoparticles, which enables in situ ED and HRTEM measurements at the single or subparticle level. The HRTEM imaging coupled with GPA (using a new algorithm as given in Materials and Methods) generates the spatial distribution of Li concentration in local areas of a single nanoparticle. STM, scanning tunneling microscope. (C) Demonstration of the high-rate capability of FP nanoparticles in the TEM grid-based electrodes. The voltage profiles are similar to those obtained from standard coin cells (fig. S2).

spatial and temporal variations of Li concentration and thus serve as a probe for the intercalation processes in local areas within a single-crystalline nanoparticle.

Nonequilibrium intercalation via solid-solution transformation

In situ ED measurements were conducted on a single FP nanoparticle during lithiation to determine the pathway of phase transformation (that is, single- or two-phase mechanisms) at the single-particle level. Time-resolved ED patterns were recorded at a frequency of two patterns per second from a selected FP nanoparticle (approximately 35 nm wide and 58 nm long; fig. S3) upon lithiation at a rate equivalent to ~ 18 C, where C is the single-particle rate (defined using a similar method in the previous work) (15). The main results are given in Fig. 2 and movie S1, wherein the nanoparticle was tilted to [010] zone axis, allowing the tracking of the changes in the a and c lattice parameters using diffraction spots of $\{200\}$ and $\{001\}$, respectively (Fig. 2A). The initial single (200) spot associated with the FP phase ($a = 9.83$ Å, $c = 4.78$ Å) gradually splits due to the formation of Li_xFePO_4 ($0 < x < 1$) as lithiation proceeded. Figure 2B shows a representative ED pattern recorded after 113 s of lithiation, corresponding to the Li_xFePO_4 with lattice parameters, $a = 10.05 \pm 0.01$ Å and $c = 4.71 \pm 0.01$ Å. The splitting of the diffraction spot is subtle because of the small lattice change, so the intensity profiles of the diffraction spots were extracted to show the gradual changes in the ED. Figure 2C shows the intensity profiles of the (200) spot as a function of lithiation time. When the lithiation started (at 0 s), the (200) peak became broadened, and with further lithiation, at about 13 s, a new, barely separated peak became visible. The gradual separation,

with the peak on the left [corresponding to a shorter distance between (200) to the central spot] continuously shifting to the left, indicates the formation of Li_xFePO_4 of increasing Li content through a continuous solid-solution transformation (36). At the end of lithiation (at ~ 203 s), the shift of the (200) peak from that of the initial FP phases corresponds to a lattice expansion of nearly 4.7%, close to the theoretical misfit of 5.0% between LFP and FP (37). The gradual decrease in the lattice parameter c was also observed from the evolution of the (001) diffraction spot (fig. S4). In addition, the reduction of Fe valence state due to lithiation was determined by EELS (via the chemical shift of Fe L-edge spectra; fig. S5). Therefore, our in situ ED measurements unambiguously identified the solid-solution transformation in a single nanoparticle of known size and morphology.

The evolution of the relative change in lattice spacing a versus lithiation time, defined by $\epsilon_a = (a_{\text{Li}_x\text{FePO}_4} - a_{\text{FP}}) / (a_{\text{LFP}} - a_{\text{FP}})$, was also extracted from the intensity profiles and plotted in Fig. 2D. The gradual increase of ϵ_a with time during the solid-solution transformation was highly nonlinear. For example, a slow increase of the lattice spacing a was observed in the intermediate stage (between 40 and 150 s), in contrast to an abrupt increase in the initial and final stages. The estimated values of the lattice spacing within the intermediate stage correspond to a Li concentration range of $x = 0.3$ to 0.6 in Li_xFePO_4 based on Vegard's law (22, 36, 38, 39), which is close to the composition between $\text{Li}_{0.25}\text{FePO}_4$ and $\text{Li}_{0.65}\text{FePO}_4$, determined by in situ XRD measurements from agglomerates of nanoparticles (11). However, the nonlinear evolution of composition during the solid-solution transformation was not observed by in situ XRD.

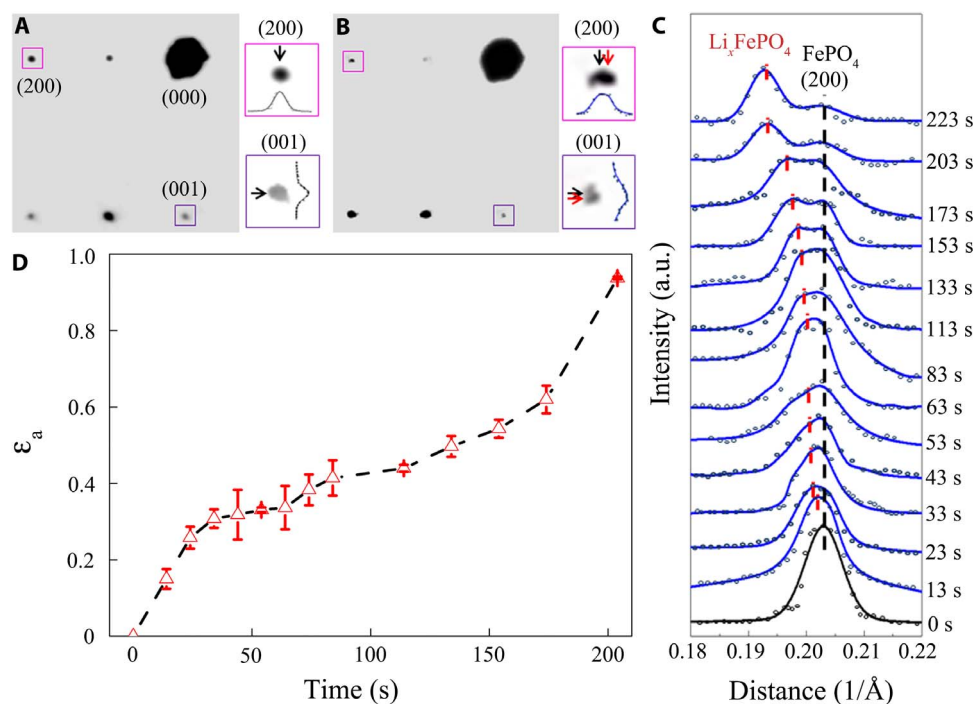


Fig. 2. In situ ED measurements indicating a solid-solution transformation in a single Li_xFePO_4 nanoparticle. Representative ED patterns recorded from a b -oriented FP nanoparticle (shown in fig. S3) at (A) the pristine state and (B) an intermediate state after 113 s of lithiation. The splitting of the (200) and (001) diffraction spots indicates the transformation from FP (marked by black arrows) to Li_xFePO_4 (red ones). (C) Evolution of intensity profiles of the (200) diffraction spots versus the distance from the center (000). Dots: original data; solid lines: fitted ones by weighted Gaussian and Lorentzian functions. (D) Evolution of relative change of lattice spacing a , defined by $\epsilon_a = (a_{\text{Li}_x\text{FePO}_4} - a_{\text{FP}}) / (a_{\text{LFP}} - a_{\text{FP}})$, where the lattice parameter $a_{\text{Li}_x\text{FePO}_4}$ was measured from the peak positions in the fitted profiles in (C) (being marked with red vertical lines), as a function of the elapsed time (shown by red triangles); the dashed curve is a guide to the eye. The error bars correspond to the standard deviation obtained from four diffraction spots $\pm(100)$ and $\pm(200)$. a.u. arbitrary unit.

Li concentration reversal within nanosized domains

Following the in situ ED examination of the lattice spacing averaged over an entire nanoparticle, in situ lattice imaging was used to further investigate the local intercalation process on another FP nanoparticle. The main results are given in Fig. 3. All of the lattice images recorded at different lithiated states from an area of about $47 \times 47 \text{ nm}^2$ (as marked by the blue box in Fig. 3A) are given in fig. S6. The lattice spacing is highly homogeneous, as demonstrated by the magnified view of the lattice image (inset in Fig. 3A; for a $10 \times 10 \text{ nm}^2$ area as marked by the red box). Fast Fourier transformation (FFT) patterns were extracted from the lattice images of the selected area to examine the evolution of the lattice spacing using a similar approach as in the in situ ED measurements. The gradual change of the lattice spacing with time (as displayed in fig. S7, A and B) is overall similar to the observations by in situ ED (Fig. 2C and fig. S4), again indicating a solid-solution transformation process, with temporal nonlinearity (that is, a relatively slower increase of lattice spacing a in the intermediate lithiation stage between 40 and 150 s). These results indicate that the FFT analyses of the HRTEM images from a portion of FP nanoparticles captured the solid-solution transformation discovered from in situ ED measurements of an entire nanoparticle. However, by comparing the FFT patterns from different areas (as illustrated in fig. S8), it can be found that the lattice displacement during a monophasic solid-solution lithiation process was signif-

icantly different from one area to another. To map the local, lithiation-driven lattice displacement in FP throughout the viewed area, a redesigned GPA method was used to process the in situ HRTEM images (detailed in Materials and Methods). During a single-phase solid-solution transformation, phase boundaries, which would manifest as an abrupt change in local coherent lattice strain, do not form, but rather one single phase of varying Li concentration forms (11, 24). Therefore, Vegard's law is applied here to convert the local lattice displacement into Li concentration distribution at different lithiation states (Fig. 3, B to I). The evolution of Li concentration shows that the solid-solution transformation proceeded continuously and heterogeneously across the entire area of view, without forming distinctive Li-poor Li_xFePO_4 ($0 < x < 0.2$) or Li-rich $\text{Li}_{1-x}\text{FePO}_4$ ($0.8 < 1 - x < 1$) phases (40, 41). Instead, only noticeable concentration gradients between neighboring regions with relatively high and low Li concentration appeared during the entire lithiation process (as shown in fig. S9). This observation is significantly different from that in micrometer-sized FP particles, in which the two distinctive phases coexist (32, 42).

Quantitative analysis was also applied to the local Li concentration distribution in Fig. 3 (B to I) by sampling the data over a certain selected area, such as A with a dimension of $3 \times 3 \text{ nm}^2$ (as illustrated in Fig. 3B). The averaged concentration in A is plotted by the red dashed curve in Fig. 3J. Surprisingly, a reversal in Li concentration over time was

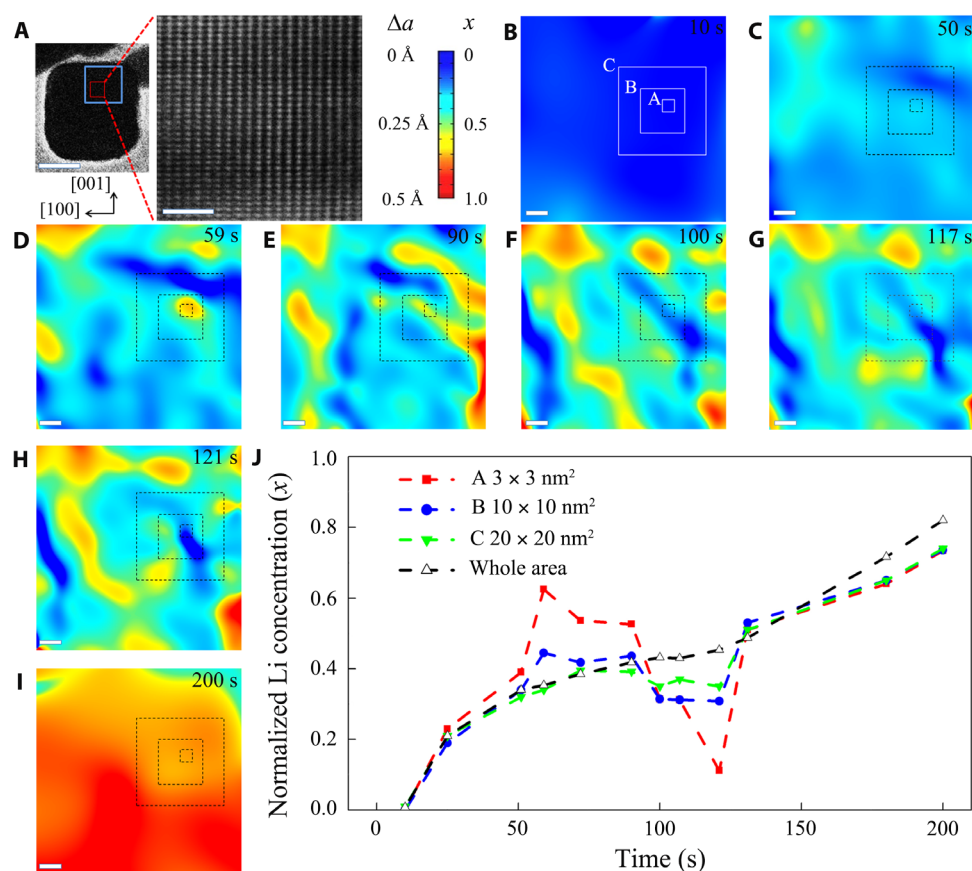


Fig. 3. Visualization of the Li concentration evolution at sub-nanoscale within a single-crystalline Li_xFePO_4 nanoparticle during lithiation (at a rate of $\sim 18 \text{ C}$). (A) Bright-field image and expanded view of the local lattice image from a single-crystalline FP nanoparticle (about 113 nm in width and 120 nm in length) at the pristine state oriented along [010] (scale bars, 50 and 5 nm, respectively). (B to I) 2D maps of local Li concentration (x in Li_xFePO_4) at a series of lithiated states for the selected area marked by the blue box in (A), which were derived from the lattice displacement of (100) planes relative to the pristine state (see fig. S6 for HRTEM images and Materials and Methods for the GPA processing). Color scale next to (B) indicates the lattice expansion Δa (relative to the lattice spacing a at the pristine state) and corresponding normalized Li concentration x . Scale bars, 5 nm. (J) Evolution of the averaged Li concentration (x) averaged over selected areas with different sizes [as marked by squares in (B) to (I)].

observed, in which the concentration increased rapidly in the early stage (up to approximately 0.6 by 59 s) and subsequently dropped to about 0.1 (at 121 s). Thereafter, the averaged Li concentration increased again, up to about 0.7 by 200 s. Multiple regions experience such Li concentration reversal within the samples examined, as demonstrated in fig. S9. Here, we note that the calculated composition may include a small error because the effect of lattice relaxation was neglected. However, if the effect of lattice relaxation is taken into account in the analysis, the amplitude of reversal in concentration will be greater. Therefore, the general conclusion is not affected when considering the effect of lattice relaxation. Furthermore, it is clear that the concentration reversal does not originate from concentration fluctuation due to thermal noise because the length scale of the concentration reversal observed in the experiment is much larger than that associated with clustering, dissolution, and nucleation for the LFP phase. The critical radius for forming an LFP nucleus, estimated following the classical nucleation theory used by Malik *et al.* (20), is ~ 0.3 nm under an apparent overpotential of 3 V, a condition corresponding to this experiment. Clusters much larger than this size are expected to grow, not dissolve, solely because of thermal fluctuation under the condition. The results thus indicate that a thermodynamic driving force underlying the concentration reversal exists.

A similar approach was applied to extract the averaged Li concentration from areas of additional sizes of data sampling, namely, 10×10 nm² and 20×20 nm² (labeled by B and C, respectively, in Fig. 3B), also showing a similar phenomenon of Li concentration reversal (Fig. 3J). However, the comparison between the curves shows a strong dependence of the Li concentration reversal on the size of the sampling areas, with an abrupt reduction of the amplitude as the sampling size was increased to 10×10 nm² (as in region B). The concentration reversal became negligibly small in region C (of 20×20 nm²), and when the sampling size was further increased to the entire area (in the blue box in Fig. 3A), the reversal was no longer observable, indicating that the concentration reversal is a highly localized phenomenon, and may be obscured when the resolution is insufficient. Another striking feature is an opposite concentration undulation in the regions adjacent to each other, for example, in the lower left corner of region B versus that in the upper left corner (fig. S10). Such an anticorrelated concentration undulation between neighboring areas is a manifestation of the intraparticle redistribution of Li. Thus, unless the imaging resolution affords the distinction between these regions with undulated concentration evolution, the concentration reversal phenomenon would not be detectable. In the recent studies of Li intercalation within a single LFP particle using in situ XRD (24) and in situ STXM techniques (15), no reversal but continuous evolution of Li concentration in the intermediates was observed, probably because of the limited spatial resolution (~ 100 nm or lower), under which the reversal became averaged out.

DISCUSSION

The localized Li concentration reversal within nanometer regions of FP nanoparticles (Fig. 3), along with the redistribution of Li (fig. S10), has not been reported in the literature to the best of the authors' knowledge. This phenomenon resembles the interparticle Li redistribution in a multiparticle system (27–30). In nanoparticulate LFP cathodes, particles lithiate differently because of different surface area-to-volume ratio (28, 29) or particle positions (19). Driven by the difference in chemical potentials between neighboring particles that have lithiated to different states, interparticle Li redistribution occurs and results in a certain degree of

concentration reversal of those lithiated particles. Analogous to such interparticle dynamics (19, 28), within a particle, some regions may lithiate faster than their surrounding areas. Hereafter, for convenience, we denote the fast-lithiating regions as Ω_α and the surrounding regions as Ω_β . The Li concentration in Ω_α (which is denoted as x^α) increases faster than x^β (the Li concentration in Ω_β) and enters the unstable spinodal range before its surroundings. Subsequently, Ω_α experiences a concentration surge, and x^α rapidly traverses from the lower spinodal to the upper spinodal point. This process can be illustrated by the magenta arrow in Fig. 4A, wherein the chemical potential function is non-monotonic because of the two-phase nature of LFP. Thereafter, when x^β enters the spinodal composition range (following the cyan arrow in Fig. 4B), x^α decreases (following the magenta arrow in Fig. 4B) because of the driving force toward the equilibration of the chemical potentials of the two regions. The value of x^α can drop to the upper spinodal point (as indicated by the black arrow in Fig. 4B), followed by a rise back to the lithiated state. In this case, the degree of concentration reversal is small and limited to the upper spinodal point when the chemical potential function is assumed to be the same for all regions in the particle. However, the experiment presented above showed a much larger concentration reversal in some regions, such as the local domain A in Fig. 3J, wherein the highly lithiated region (with concentration of ~ 0.6) experienced an abrupt decrease to the Li-poor state (with concentration of ~ 0.1).

To explain such a large concentration drop, we propose a modification to the chemical potential function of Ω_α by making it higher than that of Ω_β near the upper spinodal point. The red (μ^α) and blue (μ^β) curves in Fig. 4 (C and D) represent the chemical potential functions

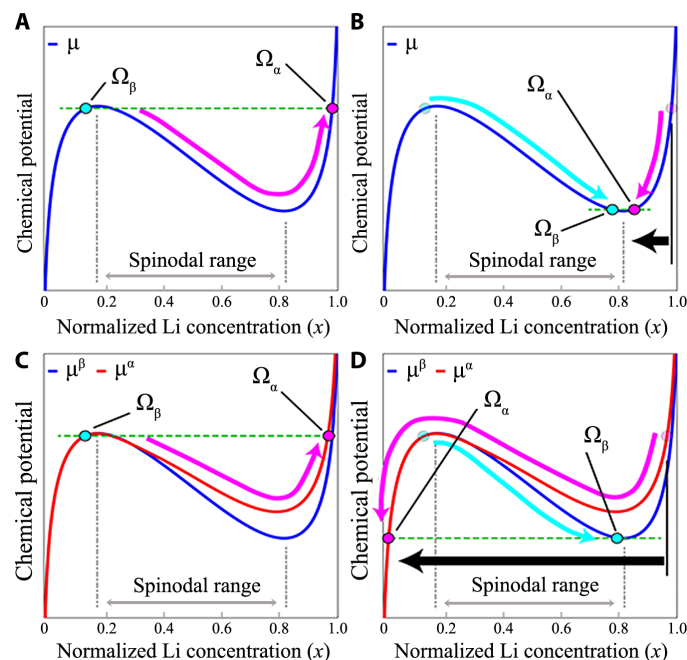


Fig. 4. Chemical potential as a function of Li concentration in fast-lithiating regions Ω_α and surrounding regions Ω_β within a single particle. (A and B) Schematics showing the mechanism for concentration reversal in Ω_α when the chemical potential function is the same for Ω_α and Ω_β . (C and D) Schematics showing the mechanism for concentration reversal in Ω_α when its chemical potential function (μ^α) has larger values than that of Ω_β (μ^β) near the upper spinodal point. The degrees of concentration reversal in the two cases are shown by the black arrows in (B) and (D). The evolution of Li concentration is indicated by the magenta and cyan arrows, respectively.

for Ω_α and Ω_β , respectively. In this scenario, x^α is able to traverse back to the delithiated state (following the magenta arrow in Fig. 4D) as x^β crosses the spinodal range (following the cyan arrow in Fig. 4D), after the fast lithiation of Ω_α seen in Fig. 4C. This large concentration drop is indicated by the black arrow in Fig. 4D. Such a large concentration drop during lithiation of the particle, spanning over the entire spinodal range as observed in the experiment, is only possible when the chemical potential functions near the upper spinodal point are different.

To verify the proposed mechanism for the large concentration reversal due to the variation in local chemical potential functions, we performed a set of 3D phase-field modeling (43) to simulate the process of intercalation. The main results are provided in Fig. 5. In this model, the evolution of the system is described by a governing equation based on the transport resulting from the chemical potential gradient. The computational domain represents a portion of a particle that contains two distinct regions, Ω_α and Ω_β , which are assumed to be static and have different free energy functions and thus different chemical potential functions (the red and blue curves in Fig. 5A). These functions are selected such that the simulated Li concentration evolution resembles the experimental observation. The function of μ^α deviates from μ^β in a degree larger than in Fig. 4 (C and D). This assumption is not un-

reasonable because the Li free energy functions are influenced by impurities and defects, which may cluster on the nanoscale regions. Thus, the free energy function could be affected over the entire Li concentration range, not just near the upper spinodal point. Note S1 provides information and discussion about the presence of clustering of anti-site defects, supported by multimodal characterizations (figs. S11 and S12). Anti-site defects can form early due to high mobility of Fe ions in FP (44). However, when the particle is fully lithiated, the migration barrier of the Fe ion in LFP is so high (1.2 eV) that the Fe ion becomes essentially immobile (44). Because we have no information on Fe mobility at the intermediate states, we take the simplifying assumption of static domains in light of the fact that little information is available on the dynamics of defect formation and clustering.

In a simplified configuration, several rectangular cuboids (representing Ω_α) were encompassed by Ω_β (Fig. 5B). In the early stage, the equilibrium of Li chemical potentials (as indicated by the black dashed line in Fig. 5A) will drive Li concentration in Ω_α (denoted as x_0^α) to be higher than that in Ω_β (denoted as x_0^β) (see Fig. 5, A and C). Once Li concentration in Ω_β exceeds the lower spinodal (x_1^β), μ^β decreases (following the cyan arrow in Fig. 5A) because of the nonmonotonic form of the chemical potential function. Driven by the difference in chemical potentials, x_1^α decreases to x_2^α

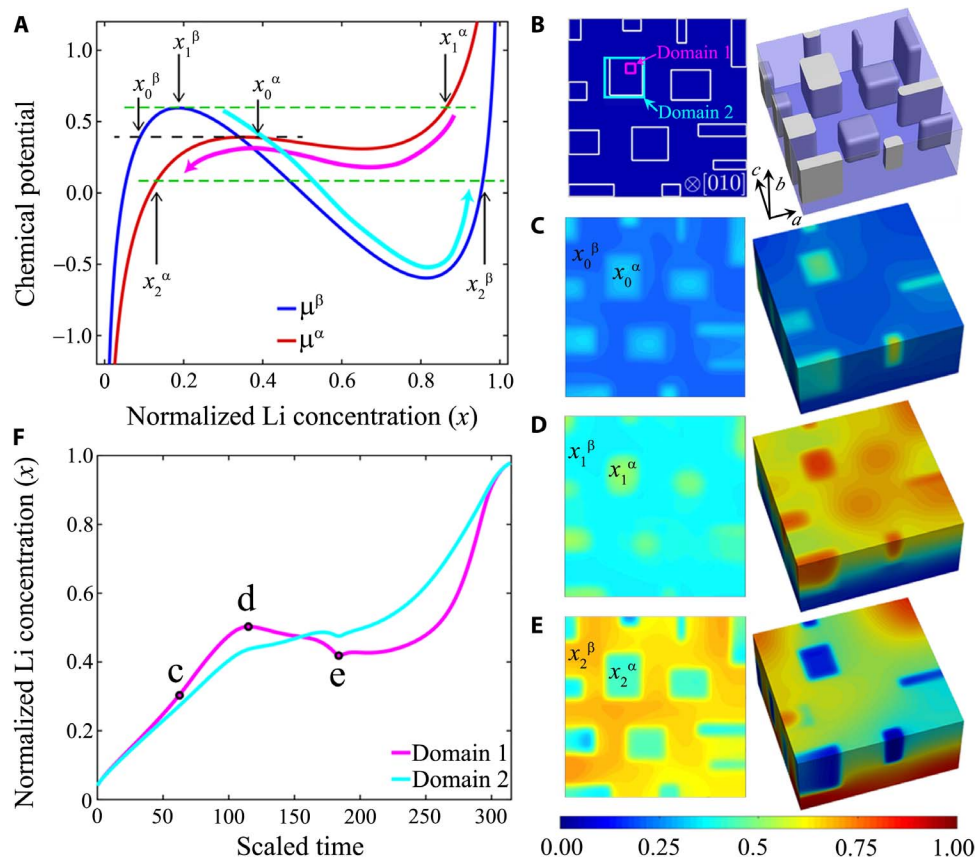


Fig. 5. Simulation of the localized concentration reversal within a single-crystalline particle using a phase-field model. (A) Chemical potential functions μ^α and μ^β versus normalized Li concentration (x) for the fast-lithiating regions Ω_α and surrounding regions Ω_β , respectively. (B to E) Snapshots of projected Li concentration along the [010] direction (left column) and the corresponding 3D view of the simulated concentration distribution (right column) at different stages of lithiation. The color scale represents Li concentration. Several cuboids marked by white boxes in (B) are assumed to be Ω_α with the modified chemical potential function, μ^α . The normalized Li concentrations of the Ω_α and Ω_β in (A) are also labeled in (C) to (E). (F) Evolution of averaged Li concentration over different sampling sizes as labeled with domains 1 and 2 in (B), which was extracted from movies S2 and S3. Domain 1 is selected to be inside Ω_α , whereas domain 2 consists of Ω_α and a part of surrounding Ω_β . The averaged concentration of domain 1 is plotted as the magenta curve that exhibits similar behavior as the experimentally examined FP nanoparticle during lithiation (Fig. 3J).

(the magenta arrow in Fig. 5A), corresponding to Fig. 5 (D and E, respectively). Consequently, x^{α} undergoes a nonmonotonic evolution during the lithiation of the nanoparticle, as shown by the magenta curve in Fig. 5F. This concentration reversal is in agreement with that observed experimentally in Fig. 3J, and thus, the simulation demonstrates that the redistribution of local Li concentration within the nanoparticles can be driven by the difference of chemical potentials between regions having different free energy functions.

The dependence of the reversal on the size of data sampling area (as illustrated in Fig. 3) can also be explained through the phase-field simulations. With an increased size of sampling volume (for example, domain 2), the lithiation of Ω_{β} offsets the concentration reversal in domain 1, resulting in a nearly monotonic overall increase in concentration (as shown by the cyan curve in Fig. 5F), which supports the experimental observation depicted in Fig. 3J.

The observation of concentration reversal in the present study serves as a critical indication of the intrinsic tendency of the FP-LFP two-phase transformation even in the absence of the distinctive phase boundaries. The nonmonotonic chemical potential function leads to the decrease of the Li chemical potential in Ω_{β} as x^{β} increases within the spinodal range, thus inducing Ω_{α} to delithiate even though overall the particle is lithiating. Intrinsic solid-solution materials, with monotonic chemical potential functions, lack the necessary driving force to reduce Li concentration of lithiated regions. Hence, the experimental observations of concentration reversal confirm that LFP nanoparticles lithiate through a metastable, nonequilibrium solid-solution pathway.

Strain energy, present due to the inhomogeneous Li distribution, may be one of the factors that would affect the amplitude of reversal. The strain energy density estimated using Li concentration distribution shown in Fig. 5D and the calculated elastic moduli and lattice parameters of FP and LFP (45) are mostly well below 5 meV per Li site, although the maximum value can approach 9 meV per Li site in a small region (fig. S13). The strain energy density overall is smaller than the calculated energy barrier for the solid solution between FP and LFP of ≈ 15 to 20 meV (20). As a result, the observed reversal phenomenon will likely remain qualitatively unchanged by strain energy. Furthermore, kinetically, it is possible that strain energy can change the migration barrier of Li (46). However, local modifications of the mobility due to strain would not induce the concentration reversal in the absence of the thermodynamic driving force. Overall, we believe that strain effect is unlikely to be the sole origin of concentration reversal.

The complex, dynamic intercalation processes observed in this study can occur in other intercalation electrode materials containing regions with different free energy functions. Although the variation in the free energy functions may appear to originate from anti-site defect clusters in LFP, similar phenomena might be observed when dopants (8), impurities, or other types of defects (47) form clusters and alter the local Li chemical potentials in other intercalation-type electrodes. However, such a phenomenon is expected to be observable only at an extremely small scale (10 nm or less), because it will be smoothed out after averaging on a larger scale. Therefore, the experimental confirmation will require extremely high-resolution techniques such as the in situ imaging coupled with GPA analysis. Additional details such as the dynamic formation of defect clusters can have an impact on the exact behavior of the concentration reversal, which may depend on the lithiation rate. To evaluate such effects quantitatively, further in situ observations of the evolution of defects within a single nanoparticle at different rates are required. However, achieving the required resolution is extremely challenging and it will be a subject of future study.

CONCLUSION

We investigated the intercalation dynamics in individual FP nanoparticles through real-time tracking of lithiation-driven structural evolution at unprecedented resolution. The local Li intercalation via kinetically favorable solid-solution pathway was unveiled at scales varying from single nanometer to tens of nanometers, and up to the entire FP nanoparticles. Despite many studies of nonequilibrium intercalation and phase transformations in nanoparticulate Li_xFePO_4 (11, 19–21, 23, 24, 36, 48), only through this work was inhomogeneous intercalation within a single nanoparticle identified. In contrast to the traditional assumption of monotonic Li incorporation within a single nanoparticle, this study revealed an unexpected reversal of the local Li concentration in nanosized domains within a particle. The discovery of inhomogeneous intercalation and localized concentration reversal of Li during intercalation into a single nanoparticle adds new insights into the existing knowledge of nonequilibrium electrochemical reactions in intercalation-type electrodes (11, 20, 23, 24).

On the basis of an assumption that different regions have different local free energy, a theory was proposed to explain the thermodynamic origin of the observed reversal phenomenon. With the thermodynamic driving force toward equilibration of the different Li chemical potentials, the local Li concentration in some regions rises by absorbing Li from its surroundings and subsequently drops when the surroundings reach spinodal composition and experience a large driving force toward lithiation. The findings from this study provide new perspective on the local dynamics of electrochemically driven phase transformations in intercalation-type battery electrodes.

MATERIALS AND METHODS

Materials synthesis and electrochemical measurements

LFP nanoparticles were synthesized using the solvothermal method (35). LiOH aqueous solution (450 ml of 1 M) was mixed with H_3PO_4 (150 ml of 1 M) and polyethylene glycol (600 ml) to form a milk-white suspension. Then, FeSO_4 solution (300 ml of 0.5 M) was added into the white suspension while stirring. The mixture was transferred into an autoclave, which was then held at 180°C for 9 hours. After cooling to room temperature, the product was collected and washed with pure water three times. The final product was dried under vacuum at 80°C for 12 hours. FP was prepared by chemical delithiation of LFP with nitronium tetrafluoroborate, NO_2BF_4 , in anhydrous acetonitrile. Typically, 1 g of LFP was immersed in 100 ml of NO_2BF_4 (5 g) in anhydrous acetonitrile for 2 days. The mixture was magnetically stirred at room temperature in an argon-filled glove box. To ensure carbon coating, the products were mixed with 17 weight % (wt %) of glucose and then carbonized at 600°C for 5 hours under an argon atmosphere with a heating rate of 5°C min^{-1} .

The TEM grid-based composite electrodes used in standard coin cells were prepared by mixing 80 wt % of LFP with 20 wt % of Super P carbon. The electrolyte was composed of a 1 M LiPF_6 solution in ethylene carbonate/dimethyl carbonate with a volume ratio of 1:1.

Structure characterization

The LFP and FP nanoparticles were characterized by x-ray using beamline X14A at the National Synchrotron Light Source (NSLS), Brookhaven National Laboratory (BNL). The TEM and annular dark-field (ADF) images were recorded in a JEOL 2100F microscope at 200 kV with a 0.23-nm point-to-point spatial resolution. The HRTEM and high-angle ADF (HAADF) images, in situ ED patterns, and EELS spectra were

recorded from the lithiated samples using a JEOL ARM 200F microscope equipped with two spherical aberration correctors, a cold field emission electron source, and a high-resolution dual-EELS spectrometer. The simulated HAADF image was calculated on the basis of the multislice method with frozen phonon approximation. During in situ ED measurements, two diffraction patterns were recorded per second, which is the same as the frequency in time-resolved XRD measurement (49). Alignment was performed in selected nanoparticles that were basically projected parallel or perpendicular to the [010] direction. The electron beam damage was minimized by spreading the electron beam to the largest beam diameter to ensure that the in situ ED measurement revealed the state of phase transformation without artifacts.

In situ HRTEM experiments

For the in situ HRTEM experiments, we used a similar design of the in situ cell as described by Wang *et al.* (17). The FP nanoparticles were loaded onto 10-nm-thick amorphous carbon films in the TEM half-grids. The carbon film has a similar role as the carbon black used in typical FP-C electrodes, acting as the media for transporting electrons and ions. A tungsten tip was used to scratch fresh Li metal from a cut Li metal surface in an argon glove box and attached to a piezo-driven biasing probe built into the TEM–scanning tunneling microscopy sample stage (Nanofactory Instruments AB). All the components were sealed in an argon glove box and transferred into the TEM column using an Ar-filled bag. As shown in Fig. 1B, the biasing probe touched the carbon, and a negative bias versus TEM half-grid (above 3 V) was applied to initiate the reaction. No reaction or current flow occurred before applying the bias, or with a lower biasing potential. The battery consisted of a TEM grid (current collector), FP-C (cathode), and Li metal (anode). A thin passivation layer of LiN_xO_y on the surface of the Li metal acted as the solid electrolyte (17).

Geometric phase analysis

GPA is a robust image-processing technique based on HRTEM images (50–52). Here, we used it to map the change in lattice spacing during phase transformation. The optical distortions caused by the projector lenses of the microscope (33) were corrected for all the GPA maps.

By applying a small mask (with the shape of one Brillouin zone) around a local Fourier component of the lattice fringes, \mathbf{g} , in the Fourier transform of a HRTEM image, we obtained the inverse Fourier transform $H_g(\mathbf{r})$ as

$$H_g(\mathbf{r}) = A_g(\mathbf{r}) \exp\{iP_g(\mathbf{r})\} \quad (2)$$

where $A_g(\mathbf{r})$ and $P_g(\mathbf{r})$ are the amplitude and phase, respectively, and \mathbf{r} is the position of the lattice fringes in the real space. $P_g(\mathbf{r})$ was used to determine the positions of the lattice fringes in real space. $H_g(\mathbf{r})$ can be related to the usual procedure to produce a Bragg filtered image, $B_g(\mathbf{r})$, which is to place a mask around the spots $\pm\mathbf{g}$ in the Fourier transform of the image and then to take its inverse Fourier transform

$$B_g(\mathbf{r}) = H_g(\mathbf{r}) \exp\{2\pi i\mathbf{g}\cdot\mathbf{r}\} + H_{-\mathbf{g}}(\mathbf{r}) \exp\{-2\pi i\mathbf{g}\cdot\mathbf{r}\} \quad (3)$$

Because the HRTEM image intensity $I(\mathbf{r})$ is a real function, $H_g(\mathbf{r}) = H_{-\mathbf{g}}^*(\mathbf{r})$, Eq. 3 becomes

$$B_g(\mathbf{r}) = 2\text{Re}[H_g(\mathbf{r})\exp\{2\pi i\mathbf{g}\cdot\mathbf{r}\}] = 2A_g(\mathbf{r})\cos\{2\pi\mathbf{g}\cdot\mathbf{r} + P_g(\mathbf{r})\} \quad (4)$$

For an image with perfectly regular set of fringes

$$B_g(\mathbf{r}) = 2A_g(\mathbf{r})\cos\{2\pi\mathbf{g}\cdot\mathbf{r} + C_g\} \quad (5)$$

where C_g is a constant. For an image with varying fringe spacing, the equation is

$$B_g(\mathbf{r}) = 2A_g(\mathbf{r})\cos\{2\pi\mathbf{g}\cdot\mathbf{r} + 2\pi\Delta\mathbf{g}\cdot\mathbf{r}\} \quad (6)$$

where $\Delta\mathbf{g}$ is the local departure from the ideal reciprocal lattice vector, \mathbf{g} . Comparing this equation with Eq. 4, we find that

$$P_g(\mathbf{r}) = 2\pi\Delta\mathbf{g}\cdot\mathbf{r} \quad (7)$$

By taking the gradient of Eq. 7, we obtain

$$\Delta\mathbf{g} = \nabla P_g(\mathbf{r})/2\pi \quad (8)$$

If we use FP as the reference lattice with lattice parameter a_{ref} along the a direction, whereas the local lattice spacing in the image is $a(\mathbf{r})$, by choosing $\mathbf{g} = 100$ in Fig. 3A, we obtain

$$\Delta\mathbf{g} = \frac{1}{a(\mathbf{r})} - \frac{1}{a_{\text{ref}}} = -\frac{a(\mathbf{r}) - a_{\text{ref}}}{a(\mathbf{r})a_{\text{ref}}} = -\frac{\Delta a}{a(\mathbf{r})a_{\text{ref}}} \quad (9)$$

Combining Eqs. 8 and 9, the change in the lattice spacing $a(\mathbf{r})$ as a function of the position and time can be expressed as

$$\Delta a(\mathbf{r}, t) = -\frac{a(\mathbf{r})a_{\text{ref}}}{2\pi} \nabla P_g(\mathbf{r}, t) \quad (10)$$

Using Vegard's law, the Li concentration shown in Fig. 3 (B to I) can be calculated to equal

$$\frac{\Delta a}{a_{\text{LFP}} - a_{\text{ref}}} = -\frac{aa_{\text{ref}}}{2\pi(a_{\text{LFP}} - a_{\text{ref}})} \nabla P_g(\mathbf{r}, t) \quad (11)$$

where a_{LFP} is the lattice parameter of LFP.

Because the difference of Li concentration between neighboring regions is in the range between 0.07 and 0.3 (fig. S9A), the differences of lattice spacing along the c direction are mostly in the range of 0.67 and 2.85 pm between neighboring regions, which is comparable to the uncertainty of the resolution limit of the GPA method of 3 pm (33). However, the difference in the lattice spacing along the a direction is in the range of 3.5 to 15 pm. Therefore, we calculated the Li concentration based on the change in the lattice spacing along the a direction.

On the basis of the uncertainty in the measured displacement of 3 pm (33), the uncertainty in the calculated local Li concentration was estimated to be 0.06. Because the HRTEM image is a projection along the b direction (through the thickness of the entire particle), the Li concentration measured in Fig. 3 is an average value along the b direction.

Phase-field simulations

A phase-field method was used to simulate the Li concentration evolution during lithiation. The concentration evolution is assumed to be governed by the Cahn-Hilliard equation (43)

$$\frac{\partial x}{\partial t} = \nabla \cdot M \nabla \bar{\mu} = \nabla \cdot M \nabla (\mu - \nabla \cdot \kappa \nabla x) \quad (12)$$

where x is the normalized Li concentration, t is the time, M is the transport mobility, $\bar{\mu}$ is the total Li chemical potential including the gradient energy penalty, μ is the chemical potential defined as the derivative of the bulk free energy with respect to concentration, and κ is the gradient energy coefficient. Equation 12 was nondimensionalized for the simulations, with a length unit $l = 1$ nm and a mobility unit $\bar{M} = 5.32 \times 10^{-12}$ cm²/s (evaluated according to the diffusivity of Li of 3.2×10^{-11} cm²/s). Thus, the time unit is 1.875×10^{-3} s ($\tau = l^2/\bar{M}$). In this model, we used two chemical potential functions for Ω_α and Ω_β

$$\mu^\alpha = 2.2(1 - 2x) + \ln(x/(1 - x)) + 0.35 \in \Omega_\alpha \quad (13a)$$

$$\mu^\beta = 3.3(1 - 2x) + \ln(x/(1 - x)) \in \Omega_\beta \quad (13b)$$

These two functions have the same form as those based on the regular solution model and are shown as the red and blue curves in Fig. 5A. Note that the regular solution chemical potential function is normalized such that the entropy term has a coefficient of unity. We assumed that the interfacial energy in the particle was isotropic and set κ_β and κ_α equal to 200 and 2, respectively, to generate comparable interfacial energy in Ω_β and Ω_α . We chose anisotropic (dimensionless) transport mobility as

$$M_a^\beta = 1 \times 10^{-4}; M_b^\beta = 1; M_c^\beta = 1 \times 10^{-4} \quad (14)$$

for Ω_β , where the subscripts denote the a , b , and c axes. For Ω_α , the mobility along the fast diffusion channels was decreased because of the assumption of the presence of high density of defects, and the anisotropy in transport properties was also lowered

$$M_a^\alpha = 1 \times 10^{-3}; M_b^\alpha = 6.5 \times 10^{-2}; M_c^\alpha = 1 \times 10^{-3} \quad (15)$$

Note that the Li diffusivity along the b axis in the Ω_β region is approximately 100 times that in Ω_α , because diffusivity is related to transport mobility by $D = M \partial \mu / \partial x$, where x is the Li fraction, and $\partial \mu / \partial x$ values are different in the two regions. In addition, because of the presence of high density of defects, it is possible that the Li mobility along a and c directions is larger than that along the b direction. In such cases, the amplitude of concentration reversal will be increased because of enhanced cross-channel Li transport. This effect was observed in the parametric study, as shown in fig. S14 and note S2.

A standard finite difference scheme was used for spatial discretization, and the forward Euler explicit time-stepping scheme was used for temporal evolution. A rectangular computational domain with dimensions of $60 \times 60 \times 30$ grid points along the a , b , and c crystalline orientations, respectively, was used in the simulations. The dimensionless grid spacing was set to be one. The Li concentration in the particle was initially uniform at 0.04 for the ease of numerical simulations. Be-

cause we only focused on the evolution of Li concentration inside the particle, instead of the voltage response during an electrochemical reaction, we did not use the Butler-Volmer equation for the insertion flux. Instead, the Li insertion rate was assumed to be proportional to the Li chemical potential difference across the particle surface. Thus, the flux boundary conditions for Li insertion were set as $J_s^b = -K(\bar{\mu} - \mu^0)$ on the two computational domain boundaries that are perpendicular to the b axis, where K is the surface reaction rate constant and μ^0 represents the Li chemical potential outside the computational domain. The value of μ^0 was kept constant, similar to a simplified constant voltage loading condition (53). The dimensionless value of K was set to be 3.125×10^{-5} to ensure near-equilibrium insertion dynamics in which the Li concentration evolution in the particle is governed by thermodynamics and diffusion kinetics. The remaining four boundaries were assumed to be within the LFP particle. Thus, no flux boundary conditions were imposed at these boundaries. Therefore, our phase-field model considered both thermodynamic driving force as well as kinetics simultaneously and consistently.

SUPPLEMENTARY MATERIALS

Supplementary material for this article is available at <http://advances.sciencemag.org/cgi/content/full/4/1/eaao2608/DC1>

movie S1. An in situ TEM movie showing the evolution of the ED patterns projected along the [010] direction.

movie S2. A simulation movie showing the evolution of projected Li concentration along the [010] direction.

movie S3. A 3D view movie showing the evolution of simulated Li concentration distribution in different local regions.

fig. S1. Morphology and structure of FP and LFP nanoparticles.

fig. S2. Electrochemical performance of FP nanoparticles tested in regular coin cells.

fig. S3. A bright-field TEM image showing a single-crystalline FP nanoparticle (in the central region), being tilted to [010] direction for in situ ED measurements (Fig. 2).

fig. S4. The evolution of ED intensity profiles of diffraction spot (001) versus distance from the central spot (000), shown with original data (dots), and fitted ones (solid lines) by weighted Gaussian and Lorentzian functions.

fig. S5. Electron energy-loss spectra of Fe-L_{2,3} and O-K edges from the FP nanoparticle (shown in fig. S3) before and after lithiation during in situ ED measurements.

fig. S6. HRTEM images from a single particle (oriented along [010]) during lithiation (as in Fig. 3) taken at different times.

fig. S7. Evolution of intensity profiles of (100) and (001) diffraction spots in the FFT patterns obtained from the HRTEM images in fig. S6, in comparison to that obtained from in situ ED measurements.

fig. S8. Local lattice displacement in FP due to lithiation.

fig. S9. Intensity profiles of the Li concentration distribution showing continuous variation of the Li concentration between the neighboring Li-rich and Li-poor regions.

fig. S10. Evolution of Li concentration averaged at the lower left and upper left corners of region B in Fig. 3 (B to I).

fig. S11. Synchrotron XRD patterns in comparison to that obtained by Rietveld refinements, from pristine LFP, chemically delithiated FP, and electrochemically lithiated LFP.

fig. S12. Inhomogeneity of anti-site defects within the electrochemically lithiated nanoparticles (LFP).

fig. S13. Calculated strain energy density on the surface of the particle and on the a - c plane at the center of the particle.

fig. S14. Evolution of averaged Li concentration over different sampling sizes (as labeled with domains 1 and 2 in Fig. 5B), with low and high anisotropic ratios of Li mobility along the three crystalline directions.

note S1. Nonuniformly distributed anti-site defects in LFP

note S2. Concentration reversal in local regions within different anisotropic ratio of Li mobility along the three crystalline directions

References (54, 55)

REFERENCES AND NOTES

1. J.-M. Tarascon, M. Armand, Issues and challenges facing rechargeable lithium batteries. *Nature* **414**, 359–367 (2001).

2. J. N. Reimers, J. Dahn, Electrochemical and in situ x-ray diffraction studies of lithium intercalation in Li_xCoO_2 . *J. Electrochem. Soc.* **139**, 2091–2097 (1992).
3. T. Ohzuku, Y. Makimura, Layered lithium insertion material of $\text{LiCo}_{1/3}\text{Ni}_{1/3}\text{Mn}_{1/3}\text{O}_2$ for lithium-ion batteries. *Chem. Lett.* **30**, 642–643 (2001).
4. M. M. Thackeray, P. J. Johnson, L. A. de Picciotto, P. G. Bruce, J. B. Goodenough, Electrochemical extraction of lithium from LiMn_2O_4 . *Mater. Res. Bull.* **19**, 179–187 (1984).
5. A. K. Padhi, K. S. Nanjundaswamy, J. B. Goodenough, Phospho-olivines as positive-electrode materials for rechargeable lithium batteries. *J. Electrochem. Soc.* **144**, 1188–1194 (1997).
6. D. B. Ravnsbæk, K. Xiang, W. Xing, O. J. Borkiewicz, K. M. Wiaderek, P. Gionet, K. W. Chapman, P. J. Chupas, Y. M. Chiang, Extended solid solutions and coherent transformations in nanoscale olivine cathodes. *Nano Lett.* **14**, 1484–1491 (2014).
7. M. S. Whittingham, Lithium batteries and cathode materials. *Chem. Rev.* **104**, 4271–4301 (2004).
8. M. S. Whittingham, Ultimate limits to intercalation reactions for lithium batteries. *Chem. Rev.* **114**, 11414–11443 (2014).
9. Y. Xia, T. Sakai, T. Fujieda, X. Q. Yang, X. Sun, Z. F. Ma, J. McBreen, M. Yoshio, Correlating capacity fading and structural changes in $\text{Li}_{1+y}\text{Mn}_{2-y}\text{O}_{4-\delta}$ spinel cathode materials: A systematic study on the effects of Li/Mn ratio and oxygen deficiency. *J. Electrochem. Soc.* **148**, A723–A729 (2001).
10. N. Yabuuchi, T. Ohzuku, Novel lithium insertion material of $\text{LiCo}_{1/3}\text{Ni}_{1/3}\text{Mn}_{1/3}\text{O}_2$ for advanced lithium-ion batteries. *J. Power Sources* **119–121**, 171–174 (2003).
11. H. Liu, F. C. Strobridge, O. J. Borkiewicz, K. M. Wiaderek, K. W. Chapman, P. J. Chupas, C. P. Grey, Capturing metastable structures during high-rate cycling of LiFePO_4 nanoparticle electrodes. *Science* **344**, 1252817 (2014).
12. Y.-N. Zhou, J.-L. Yue, E. Hu, H. Li, L. Gu, K.-W. Nam, S.-M. Bak, X. Yu, J. Liu, J. Bai, E. Dooryhee, Z.-W. Fu, X.-Q. Yang, High-rate charging induced intermediate phases and structural changes of layer-structured cathode for lithium-ion batteries. *Adv. Energy Mater.* **6**, 1600597 (2016).
13. Y.-S. Yu, C. Kim, Y. Liu, A. van der Ven, Y. S. Meng, R. Kostecki, J. Cabana, Nonequilibrium pathways during electrochemical phase transformations in single crystals revealed by dynamic chemical imaging at nanoscale resolution. *Adv. Energy Mater.* **5**, 1402040 (2015).
14. A. Singer, A. Ulvestad, H.-M. Cho, J. W. Kim, J. Maser, R. Harder, Y. S. Meng, O. G. Shpyrko, Nonequilibrium structural dynamics of nanoparticles in $\text{LiNi}_{1/2}\text{Mn}_{3/2}\text{O}_4$ cathode under operando conditions. *Nano Lett.* **14**, 5295–5300 (2014).
15. J. Lim, Y. Li, D. H. Alsem, H. So, S. C. Lee, P. Bai, D. A. Cogswell, X. Liu, N. Jin, Y.-S. Yu, N. J. Salmon, D. A. Shapiro, M. Z. Bazant, T. Tylliszczak, W. C. Chueh, Origin and hysteresis of lithium compositional spatiodynamics within battery primary particles. *Science* **353**, 566–571 (2016).
16. T. R. Ferguson, M. Z. Bazant, Phase transformation dynamics in porous battery electrodes. *Electrochim. Acta* **146**, 89–97 (2014).
17. F. Wang, H.-C. Yu, M.-H. Chen, L. Wu, N. Pereira, K. Thornton, A. Van der Ven, Y. Zhu, G. G. Amatucci, J. Graetz, Tracking lithium transport and electrochemical reactions in nanoparticles. *Nat. Commun.* **3**, 1201 (2012).
18. A. S. Aricò, P. Bruce, B. Scrosati, J.-M. Tarascon, W. Van Schalkwijk, Nanostructured materials for advanced energy conversion and storage devices. *Nat. Mater.* **4**, 366–377 (2005).
19. R. Malik, A. Abdellahi, G. Ceder, A critical review of the Li insertion mechanisms in LiFePO_4 electrodes. *J. Electrochem. Soc.* **160**, A3179–A3197 (2013).
20. R. Malik, F. Zhou, G. Ceder, Kinetics of non-equilibrium lithium incorporation in LiFePO_4 . *Nat. Mater.* **10**, 587–590 (2011).
21. P. Bai, D. A. Cogswell, M. Z. Bazant, Suppression of phase separation in LiFePO_4 nanoparticles during battery discharge. *Nano Lett.* **11**, 4890–4896 (2011).
22. M. Hess, T. Sasaki, C. Villevieille, P. Novák, Combined operando x-ray diffraction-electrochemical impedance spectroscopy detecting solid solution reactions of LiFePO_4 in batteries. *Nat. Commun.* **6**, 8169 (2015).
23. X. Zhang, M. van Hulzen, D. P. Singh, A. Brownrigg, J. P. Wright, N. H. van Dijk, M. Wagemaker, Rate-induced solubility and suppression of the first-order phase transition in olivine LiFePO_4 . *Nano Lett.* **14**, 2279–2285 (2014).
24. X. Zhang, M. van Hulzen, D. P. Singh, A. Brownrigg, J. P. Wright, N. H. van Dijk, M. Wagemaker, Direct view on the phase evolution in individual LiFePO_4 nanoparticles during Li-ion battery cycling. *Nat. Commun.* **6**, 8333 (2015).
25. A. Abdellahi, O. Akyildiz, R. Malik, K. Thornton, G. Ceder, The thermodynamic stability of intermediate solid solutions in LiFePO_4 nanoparticles. *J. Mater. Chem. A* **4**, 5436–5447 (2016).
26. J. Niu, A. Kushima, X. Qian, L. Qi, K. Xiang, Y.-M. Chiang, J. Li, In situ observation of random solid solution zone in LiFePO_4 electrode. *Nano Lett.* **14**, 4005–4010 (2014).
27. B. Orvananos, T. R. Ferguson, H.-C. Yu, M. Z. Bazant, K. Thornton, Particle-level modeling of the charge-discharge behavior of nanoparticulate phase-separating Li-ion battery electrodes. *J. Electrochem. Soc.* **161**, A535–A546 (2014).
28. B. Orvananos, R. Malik, H.-C. Yu, A. Abdellahi, C. P. Grey, G. Ceder, K. Thornton, Architecture dependence on the dynamics of nano- LiFePO_4 electrodes. *Electrochim. Acta* **137**, 245–257 (2014).
29. B. Orvananos, H.-C. Yu, A. Abdellahi, R. Malik, C. P. Grey, G. Ceder, K. Thornton, Kinetics of nanoparticle interactions in battery electrodes. *J. Electrochem. Soc.* **162**, A965–A973 (2015).
30. B. Orvananos, H.-C. Yu, R. Malik, A. Abdellahi, C. P. Grey, G. Ceder, K. Thornton, Effect of a size-dependent equilibrium potential on nano- LiFePO_4 particle interactions. *J. Electrochem. Soc.* **162**, A1718–A1724 (2015).
31. M. Jagannathan, K. R. Chandran, Analytical modeling and simulation of electrochemical charge/discharge behavior of Si thin film negative electrodes in Li-ion cells. *J. Power Sources* **247**, 667–675 (2014).
32. Y. Zhu, J. W. Wang, Y. Liu, X. Liu, A. Kushima, Y. Liu, Y. Xu, S. X. Mao, J. Li, C. Wang, J. Y. Huang, In situ atomic-scale imaging of phase boundary migration in FePO_4 microparticles during electrochemical lithiation. *Adv. Mater.* **25**, 5461–5466 (2013).
33. M. J. Hytch, J.-L. Pataux, J.-M. Pénisson, Measurement of the displacement field of dislocations to 0.03 Å by electron microscopy. *Nature* **423**, 270–273 (2003).
34. L. Gu, C. Zhu, H. Li, Y. Yu, C. Li, S. Tsukimoto, J. Maier, Y. Ikuhara, Direct observation of lithium staging in partially delithiated LiFePO_4 at atomic resolution. *J. Am. Chem. Soc.* **133**, 4661–4663 (2011).
35. S. Yang, X. Zhou, J. Zhang, Z. Liu, Morphology-controlled solvothermal synthesis of LiFePO_4 as a cathode material for lithium-ion batteries. *J. Mater. Chem.* **20**, 8086–8091 (2010).
36. P. Gibot, M. Casas-Cabanas, L. Laffont, S. Levasseur, P. Carlach, S. Hamelet, J.-M. Tarascon, C. Masquelier, Room-temperature single-phase Li insertion/extraction in nanoscale Li_xFePO_4 . *Nat. Mater.* **7**, 741–747 (2008).
37. N. Meethong, H.-Y. S. Huang, S. A. Speakman, W. C. Carter, Y.-M. Chiang, Strain accommodation during phase transformations in olivine-based cathodes as a materials selection criterion for high-power rechargeable batteries. *Adv. Funct. Mater.* **17**, 1115–1123 (2007).
38. N. Sharma, X. Guo, G. Du, Z. Guo, J. Wang, Z. Wang, V. K. Peterson, Direct evidence of concurrent solid-solution and two-phase reactions and the nonequilibrium structural evolution of LiFePO_4 . *J. Am. Chem. Soc.* **134**, 7867–7873 (2012).
39. C. Delacourt, P. Poizot, J.-M. Tarascon, C. Masquelier, The existence of a temperature-driven solid solution in Li_xFePO_4 for $0 \leq x \leq 1$. *Nat. Mater.* **4**, 254–260 (2005).
40. A. Yamada, H. Koizumi, S.-I. Nishimura, N. Sonoyama, R. Kanno, M. Yonemura, T. Nakamura, Y. Kobayashi, Room-temperature miscibility gap in Li_xFePO_4 . *Nat. Mater.* **5**, 357–360 (2006).
41. N. Meethong, H.-Y. S. Huang, W. C. Carter, Y.-M. Chiang, Size-dependent lithium miscibility gap in nanoscale $\text{Li}_{1-x}\text{FePO}_4$. *Electrochem. Solid State Lett.* **10**, A134–A138 (2007).
42. G. Chen, X. Song, T. J. Richardson, Electron microscopy study of the LiFePO_4 to FePO_4 phase transition. *Electrochem. Solid State Lett.* **9**, A295–A298 (2006).
43. J. W. Cahn, J. E. Hilliard, Free energy of a nonuniform system. I. Interfacial free energy. *J. Chem. Phys.* **28**, 258–267 (1958).
44. C. Kuss, G. Liang, S. B. Schougaard, Atomistic modeling of site exchange defects in lithium iron phosphate and iron phosphate. *J. Mater. Chem.* **22**, 24889–24893 (2012).
45. T. Maxisch, G. Ceder, Elastic properties of olivine Li_xFePO_4 from first principles. *Phys. Rev. B* **73**, 174112 (2006).
46. C. Tealdi, J. Heath, M. S. Islam, Feeling the strain: Enhancing ionic transport in olivine phosphate cathodes for Li- and Na-ion batteries through strain effects. *J. Mater. Chem. A* **4**, 6998–7004 (2016).
47. F. C. Strobridge, H. Liu, M. Leskes, O. J. Borkiewicz, K. M. Wiaderek, P. J. Chupas, K. W. Chapman, C. P. Grey, Unraveling the complex delithiation mechanisms of olivine-type cathode materials, $\text{LiFe}_x\text{Co}_{1-x}\text{PO}_4$. *Chem. Mater.* **28**, 3676–3690 (2016).
48. R. Malik, D. Burch, M. Bazant, G. Ceder, Particle size dependence of the ionic diffusivity. *Nano Lett.* **10**, 4123–4127 (2010).
49. Y. Orikasa, T. Maeda, Y. Koyama, H. Murayama, K. Fukuda, H. Tanida, H. Arai, E. Matsubara, Y. Uchimoto, Z. Ogumi, Transient phase change in two phase reaction between LiFePO_4 and FePO_4 under battery operation. *Chem. Mater.* **25**, 1032–1039 (2013).
50. M.-W. Chu, I. Szafraniak, R. Scholz, C. Harnagea, D. Hesse, M. Alexe, U. Gösele, Impact of misfit dislocations on the polarization instability of epitaxial nanostructured ferroelectric perovskites. *Nat. Mater.* **3**, 87–90 (2004).
51. M. J. Hytch, Analysis of variations in structure from high resolution electron microscope images by combining real space and Fourier space information. *Microsc. Microanal. Microstruct.* **8**, 41–57 (1997).
52. A. Nie, L.-Y. Gan, Y. Cheng, H. Asayesh-Ardakani, Q. Li, C. Dong, R. Tao, F. Mashayek, H.-T. Wang, U. Schwingenschlöggl, R. F. Klie, R. S. Yassar, Atomic-scale observation of lithiation reaction front in nanoscale SnO_2 materials. *ACS Nano* **7**, 6203–6211 (2013).

53. H.-C. Yu, C. Ling, J. Bhattacharya, J. C. Thomas, K. Thornton, A. Van der Ven, Designing the next generation high capacity battery electrodes. *Energy Environ. Sci.* **7**, 1760–1768 (2014).
54. L. Laffont, C. Delacourt, P. Gibot, M. Yue Wu, P. Kooyman, C. Masquelier, J. Marie Tarascon, Study of the LiFePO₄/FePO₄ two-phase system by high-resolution electron energy loss spectroscopy. *Chem. Mater.* **18**, 5520–5529 (2006).
55. Y. Janssen, D. Santhanagopalan, D. Qian, M. Chi, X. Wang, C. Hoffmann, Y. S. Meng, P. G. Khalifah, Reciprocal salt flux growth of LiFePO₄ single crystals with controlled defect concentrations. *Chem. Mater.* **25**, 4574–4584 (2013).

Acknowledgments

Funding: This work was partially supported by the NorthEast Center for Chemical Energy Storage, an Energy Frontier Research Center funded by the U.S. Department of Energy (DOE), Office of Science, under award nos. DE-SC0001294 and DE-SC0012583 (H.-C.Y., H.L., A.A., B.O., F.C.S., G.C., K.T., C.P.G., and F.W.) and by the Laboratory Directed Research and Development program at the BNL, under contract no. DE-SC0012704. Efforts by W.Z. and F.W. involving the detailed analysis of the data for Fig. 3 and fig. S9 and overall writing and revision of the manuscript were supported by the Center for Mesoscale Transport Properties, an Energy Frontier Research Center supported by the U.S. DOE, Office of Science, Basic Energy Sciences, under award no. DE-SC0012673. Efforts on GPA analysis by L.W. and Y.Z. were supported by the U.S. DOE, Office of Basic Energy Science, Division of Materials Science and Engineering under contract no. DE-SC0012704. Efforts on sample preparation and electrochemical tests by B.Q., X.Z., and Z.L. were supported by National Key R&D Program of China (grant no. 2016YFB0100100), Strategic Priority Research Program of Chinese Academy of Sciences (CAS; grant no. XDA09010101), and the Key Projects in Cooperation between CAS and U.S. DOE (grant no. 174433KYSB20150047). The TEM and XRD measurements carried out in part at the Center for Functional Nanomaterials and the NSLS at BNL, respectively, were supported by the U.S. DOE, Office of Basic Energy Sciences, under contract no. DE-SC0012704. Computational resources

were provided by the Extreme Science and Engineering Discovery Environment (allocation no. TG-DMR110007), which was supported by NSF grant no. ACI-1053575, the National Energy Research Scientific Computing Center, a DOE Office of Science User Facility supported by the Office of Science of the U.S. DOE under contract no. DE-AC02-05CH11231, and the University of Michigan Advanced Research Computing. **Author contributions:** F.W. and C.P.G. initiated the project. F.W. and W.Z. conceived the experiments. W.Z. conducted the measurements and analyzed the data. H.-C.Y., B.O., and K.T. developed the phase-field model described above and performed simulations. L.W. and Y.Z. wrote the program for GPA analysis and assisted with the data analysis of HRTEM, HAADF, and ED. J.B. assisted with the XRD experiments and made the XRD refinement. H.L., F.C.S., and C.P.G. prepared samples for early in situ TEM measurements and assisted with data interpretation. A.A. and G.C. assisted with data interpretation and provided important insights into the phase transformation mechanisms. B.Q., X.Z., and Z.L. synthesized samples and made electrochemical measurements. W.Z., H.-C.Y., K.T., and F.W. wrote the paper, and all authors were involved in revising the manuscript. **Competing interests:** The authors declare that they have no competing interests. **Data and materials availability:** All data needed to evaluate the conclusions in the paper are present in the paper and/or the Supplementary Materials. Additional data related to this paper may be requested from the authors.

Submitted 30 June 2017

Accepted 4 December 2017

Published 12 January 2018

10.1126/sciadv.aao2608

Citation: W. Zhang, H.-C. Yu, L. Wu, H. Liu, A. Abdellahi, B. Qiu, J. Bai, B. Orvananos, F. C. Strobridge, X. Zhou, Z. Liu, G. Ceder, Y. Zhu, K. Thornton, C. P. Grey, F. Wang, Localized concentration reversal of lithium during intercalation into nanoparticles. *Sci. Adv.* **4**, eaao2608 (2018).